Journal of Geophysical Research: Space Physics

RESEARCH ARTICLE
10.1029/2018JA025264

Observation of Ionospheric Alfvén Resonances at 1–30 Hz and Their Superposition With the Schumann Resonances

C. D. Beggan[1] and M. Musur[1]

[1] British Geological Survey, Edinburgh, UK

Key Points:
- Schumann and ionospheric Alfvén resonances are detected in search coil measurements in the United Kingdom from September 2012 to September 2017
- During winter, in particular, the two resonance types overlap showing superposition in dynamic spectrograms across frequencies between 1 and 30 Hz
- The occurrence of this interaction between the resonances is strongly linked to season and the geomagnetic activity cycle

Correspondence to:
C. D. Beggan,
ciar@bgs.ac.uk

Citation:
Beggan, C. D., & Musur, M. (2018). Observation of ionospheric Alfvén resonances at 1–30 Hz and their superposition with the Schumann resonances. *Journal of Geophysical Research: Space Physics*, *123*. https://doi.org/10.1029/2018JA025264

Received 24 JAN 2018
Accepted 22 APR 2018
Accepted article online 9 MAY 2018

Abstract Long-term measurements of the high-frequency magnetic field (0.1–100 Hz) have been made at Eskdalemuir Observatory in the United Kingdom since September 2012. We analyze five years of dynamic spectrograms to examine the occurrence and behavior of the Schumann and ionospheric Alfvén resonances (IAR) and Pc1 pulsations. The resonances, observed as diffuse bands, arise from reflections of energy both within the Earth-ionosphere cavity and from the nonlinear conductivity gradient of the ionosphere. Schumann Resonances (SR) occur continuously but IAR are observed to arise at local nighttime in ~50% of days in the data set. Typically, IAR are found at frequencies of 1–8 Hz, but we find them extending out to 30 Hz and strongly superimposing over the first three Schumann resonances around 9% of the time. These phenomena include constructive and destructive interference, nonlinear frequency changes over the span of several hours, and polarity enhancements. In addition, the magnitude of the IAR does not decline rapidly with frequency as often proposed. We find that the IAR and their superposition with SR are strongly controlled by season and geomagnetic activity. We compare 6 days with the most unusual IAR behavior in the data set to ionosonde measurements of f_0F_2, a proxy for ionospheric conductivity but find little correlation. We suggest that, as current theoretical modeling does not account for these observations, further work is needed to understand how they arise.

Plain Language Summary Measurements of the very rapid changes of the Earth's magnetic field (changes at a rate of between 1 and 50 times per second) show very weak repeating patterns. They are caused by magnetic fields from lightning strikes in thunderstorms near the equator. The lightning strikes are strong enough to "echo" around the globe repeatedly for a few seconds before fading, similar to the sound from a resonating bell. These patterns repeat at fixed periods of around 8, 14, and 21 times per second and are called the Schumann resonances. At night time, other patterns appear in the measurements caused by magnetic waves temporarily trapped in the upper atmosphere (called the ionosphere) between heights of 100 and 1,000 km. These patterns are labeled the ionospheric Alfvén resonances are a relatively unstudied feature of the Earth's magnetic field. We looked at these patterns in magnetic field data collected from Eskdalemuir Observatory in the United Kingdom over the past 5 years. We checked how often these types of patterns occurred and found a link to the seasons and how active, in general, the magnetic field is. We also found unusual and currently unexplained patterns including interference between the Schumann and ionospheric Alfvén resonances.

1. Introduction

Induction coil magnetometers allow the measurement of small and very rapid changes of the magnetic field at the pT (10^{-12} T) level. A set of two perpendicular horizontal coils at Eskdalemuir Observatory in the Scottish Borders of the United Kingdom have been recording magnetic field variations over an effective frequency range of 0.1–50 Hz since September 2012. The extremely low frequency (ELF) band encompasses phenomena such as the Schumann resonances (SR) and ionospheric Alfvén resonances (IAR), as well as magnetospheric pulsations, which are observable in the dynamic power spectrum of the magnetic field. Such resonances arise from energy reflection within the inhomogeneous structure of the Earth-ionosphere and ionosphere-magnetosphere systems.

The Schumann resonances are created from the continuous broadband emission of electromagnetic (EM) energy from global lightning strikes (Schumann, 1952). The majority of lightning occurs close to the equatorial regions, trailing the subsolar point, as large convective clouds form thunderstorms during the afternoon heat.

Part of the EM energy is trapped by the Earth-ionosphere cavity which allows fixed bands of harmonics with wavelengths approximately divisible by the Earth's circumference to oscillate for a few seconds before dissipation. The SR are formed at frequencies around $f_n = c/2\pi a \cdot \sqrt{n(n+1)}$, where n is the harmonic, c is the speed of light, and a is the radius of the Earth. However, as this formula is for an idealized cavity, in reality the finite conductivity of the ionosphere means that the measured resonance frequencies do not match the theoretical values (Nickolaenko & Hayakawa, 2002). The low quality of the cavity ($Q \sim 4$) reduces the frequencies of the SR below their theoretical values. As a result the first six resonances in the United Kingdom are found around 7.9, 14.0, 20.1, 26.5, 32.4, and 37.5 Hz (e.g., Füllekrug, 1995).

The SR display an obvious diurnal variation, strengthening as the subsolar point crosses the three main continental regions (Asia, Africa, and America; e.g., Sátori, 1996). They also display strong seasonal and solar cycle dependencies in addition to other atmospheric variations such as the El Niño–Southern Oscillation and Madden-Julian Oscillation (Anyamba et al., 2000; Sátori, 1996; Sátori et al., 2005; Williams, 1992). The controlling factors for seasonal and atmospheric variations are changes in the location and intensity of the lightning centers, while the solar cycle changes are due to variation in the solar X-ray flux which changes the conductivity profile within the E region. The conductivity varies by an order of magnitude over the solar cycle and modulates the dissipation effects within the ionosphere, also affecting the Q-factor (Nickolaenko et al., 2015; Sátori et al., 2005).

The ionospheric Alfvén resonances are typically detectable in the 0.5–10 Hz region of the magnetic field spectrum (Belyaev et al., 1989). They arise primarily from the partial reflection of energy in the ionosphere excited along magnetic field lines by the leakage of electric fields, most likely associated with terrestrial lightning activity (Füllekrug & Reising, 1998; Greifinger & Greifinger, 1968; Nosé et al., 2017). The waves reflect off the "walls" of the E region and $F2$ region where the gradients of electron density reach a maximum (Belyaev et al., 1990). This partial reflection sets up a series of resonant frequencies along the field lines, giving rise to three or more harmonics, which are visible as a series of fringes in dynamic spectrograms of the magnetic field as measured on the ground. The IAR occur at local nighttime, beginning at low frequency and spreading out to higher frequencies until around midnight before converging back to lower frequencies by sunrise (Potapov et al., 2014).

As an interesting geophysical phenomenon, they have been extensively studied and modeled to understand their origin (e.g., Fedorov et al., 2016; Lysak, 1991, 1993). In terms of observations, Belyaev et al. (1999) looked at the properties of IAR at high latitude ($L > 5$), while Bösinger et al. (2002, 2004) examined them at low latitudes ($L = 1.3$). Work by Yahnin et al. (2003), Hebden et al. (2005), and Parent et al. (2010) found that the IAR were anticorrelated with geomagnetic activity, for example. Further research by Nosé et al. (2017) with magnetometer data from Japan again confirmed that the IAR are a local nighttime phenomena, with peak occurrence before midnight and have a strong seasonal dependence, being most common in winter months. In addition, the peak-to-peak difference between the IAR fringes also changes with season and is largest in winter at 0.5–0.7 Hz but smaller in summer and the equinoxes (cf. Beggan, 2014).

Hebden et al. (2005) and Potapov et al. (2014) examined the link between the characteristics of the discrete spectral bands and the conductivity of the ionosphere through the relation of IAR frequency (f) and peak-to-peak frequency (Δf) with f_0F_2 values, a measure of the critical frequency of the $F2$ layer as derived from ionosonde data. Both studies showed the high correlation of f and Δf with f_0F_2, which allows other parameters, such as the effective thickness of the ionosphere, to be derived from a combination of IAR and f_0F_2 data during geomagnetically quiet periods.

Having accumulated over 5 years of induction coil data at Eskdalemuir, a thorough examination was made to confirm the properties and characteristics described in the above cited studies. During the preparation of the dynamic spectrograms, it was noted that under certain conditions, the IAR were not confined to 1–10 Hz but extended, on occasion, to frequencies above 30 Hz. In addition, we noted periods of clear constructive and destructive interference of IAR fringes and the first three SR. We also observed patterns of nonlinear variations of the IAR frequencies, giving rise to "wavy" features in the spectra, as well as cooccurrence of the resonances with Pc1-type pulsations.

A brief mention of IAR up to 40 Hz was found in Baru et al. (2016) but without further detail. We are also aware of presently unpublished work with CARISMA induction coil data (Mann et al., 2008). However, to our

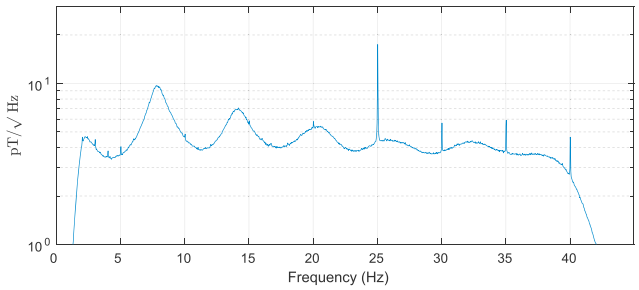

Figure 1. Average of 864 Welch periodograms for 24 hr from 12:00 2 December 2013 at Eskdalemuir, United Kingdom, from CH1.

knowledge, these two phenomena have not been previously investigated in much detail. Hence, this study presents and examines IAR features that manifest at frequencies at or above the first Schumann Resonance (>8 Hz).

In section 2 we describe the data and instrumentation at Eskdalemuir, before exploring the IAR and SR superposition in dynamic spectra in section 3. We compare the occurrence of IAR, IAR which interact with SR and pulsations over the 5 years of data collected. We also investigate seven different days as examples of unusual behavior of IAR and compare the observed IAR in the spectrograms with measurements of f_0F_2 from two ionosondes in the United Kingdom. We discuss the results in section 4 before concluding in section 5.

2. Data and Instrumentation

In June 2012, the British Geological Survey Geomagnetism team installed two horizontal perpendicular high-frequency induction coil magnetometers at the Eskdalemuir Observatory in the Scottish Borders of the United Kingdom, sited at $\theta_{geo} = 55.3°$N, $\phi_{geo} = -3.2°$E. At 2018.0, the geomagnetic location of Eskdalemuir was $\theta_{gm} = 57.5°$N in quasi-dipole coordinates with $L = 3.46$. The Eskdalemuir Observatory is one of the longest running geophysical sites in the United Kingdom, beginning operation in 1908, and is located in an isolated rural valley with a generally quiet magnetic environment away from rail lines and strong EM interference (e.g., telecommunication masts).

The instrumentation consists of two refurbished CM11-E induction coil magnetometers, orientated to north–south and east–west relative to magnetic north (the declination angle was −3.2° in 2012.5). The coils are sited away from man-made interference at the northern edge of the observatory grounds in the center of an open field. They were laid on a leveled gravel bed and covered by a wooden frame to shield them from rain and wind. A 24-bit Guralp digitizer converts the output analog signal from the coils for wired transmission to a logger located in a vault approximately 150 m away. The data are recorded at a cadence of 100 Hz by a local computer where they are time-stamped each second using Global Positioning System signals. The data are automatically collected from Eskdalemuir every 5 min and permanently stored on the British Geological Survey computer network in Edinburgh. Since September 2012 the system has run almost continuously, losing 91 days of data due to computer issues or component failure (>95% availability). The longest missing periods are 32 days between 16 November and 17 December 2014, and 19 days in July 2015.

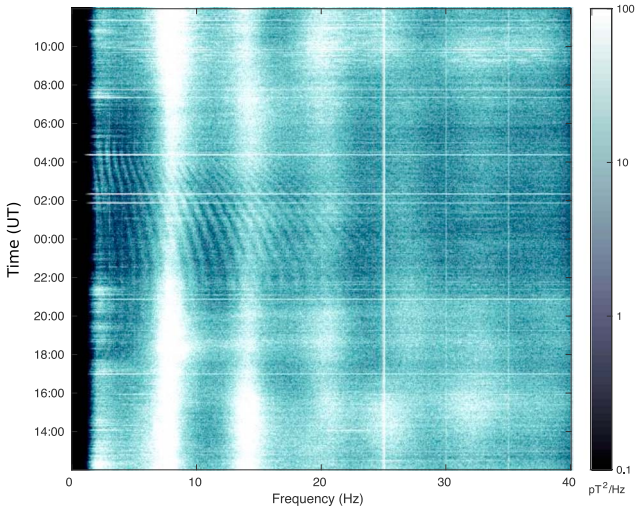

Figure 2. Spectrogram for 2–3 December 2013 from the north to south coil (CH1) showing ionospheric Alfvén resonances intersecting and interfering with the first three Schumann resonances.

The raw data are analyzed in the frequency domains using Welch periodograms (Welch, 1967). To compute a dynamic spectrogram, we perform the following steps: (1) we select a single day of data from local noon (12:00 UT) on one day to noon on the following day, (2) apply a Butterworth five-pole filter with a bandpass between 2 and 40 Hz, (3) from which a series of fast Fourier transforms are computed using the Welch method with 100 s of filtered data to produce 864 1-D spectra plots per day. A 4,096-point Fourier transform length is used on the input data (of 10,000 points) with a Hanning window to taper the data. An overlap of 100 points between windows is employed.

The individual periodograms are converted to SI units using the instrument response and digitizer calibration values. The analog coils have a relatively flat response of around 50 mV/nT between 0.1 and 100 Hz. The digitizer has a fixed conversion factor of 3.491 μV/count for the north–south channel (CH1) and 3.475 μV/count for the east–west channel (CH2). This gives a digitization level of around 0.07 pT/count for both coils for short-period signals. Figure 1 shows the average of 864 periodograms for 1 day from 12:00, 2 December to 12:00, 3 December 2013. Note the wide Schumann Resonance peaks reaching around 10 pT/$\sqrt{\text{Hz}}$ for the first resonance and the large 25 Hz subharmonic of the UK power system. The Butterworth filter causes the strong roll-off below 2 Hz and above 40 Hz.

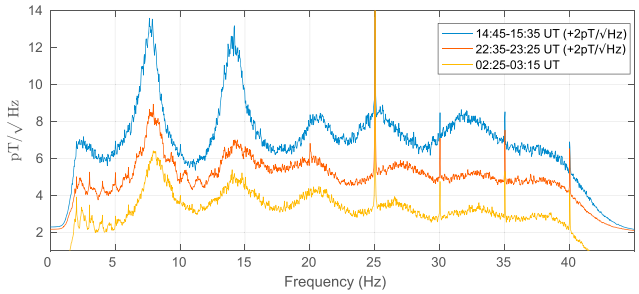

Figure 3. Average of 30 periodograms for three selected time intervals 2–3 December 2013 from CH1 coil, derived from the spectrogram in Figure 2. The upper two lines are offset from their true values for clarity.

Other subharmonics occur on the integers divisible by five arising from clipping by the fast Fourier transform processing and/or from the power grid itself (e.g., 50 Hz/3 = 16.667 Hz).

3. Observations of SR and IAR at Eskdalemuir

To create the daily spectrograms, we place the 864 individual periodograms into a matrix and take the logarithm for display purposes. Figure 2 shows an example spectrogram for the 24-hr period beginning at 12:00 UT on 2 December 2013. Time is on the vertical axis from midday to midday and frequency is along the horizontal axis (0.02–40 Hz). The six SR are seen as diffuse vertical bands and the power grid subharmonic is a thin line at 25 Hz. The horizontal lines are due to the effect of regional lightning strikes causing a large value in the raw data, which generates a large offset in the individual periodogram. The color scale indicates intensity in pT^2/Hz. From around 21:00 to 04:00 UT, the IAR can be observed to interfere with the first three SR to varying extent.

The spectrogram shows IAR fringes beginning to appear around 18:00 UT at low frequencies around 5–8 Hz. At around 22:00 UT the IAR become easily visible between 4 and 20 Hz. The Δf remains relatively constant at 0.8 Hz until 02:00 UT before the IAR decrease and fade away completely around 06:00 UT. As the SR weakens post-midnight, the IAR can be seen to intersect and overprint the first three SR between 01:00 UT and 04:00 UT, after which the IAR above 8 Hz fade away again. The same features occur in both coils.

As the IAR are quasi-stationary over periods of a few tens of minutes, the individual fringes are not visible in the daily averaged periodogram shown in Figure 1. In Figure 3 we show the average of 30 periodograms from three different time intervals: 14:45–15:35 UT and 22:35–23:25 UT on 2 December and 02:25–03:15 UT on 3 December 2013. The (blue) line from the afternoon period shows strong SR with no sign of IAR. For the late evening (red) line, the IAR are now visible as peaks with a magnitude ~ 1 pT/$\sqrt{\text{Hz}}$, superimposed on the Schumann resonances. In the early morning (orange) line, the IAR are only visible between 2 and 6 Hz, though in the spectrogram they angle sharply across the SR during this period. Note that the plots are noisier compared to Figure 1 as we have averaged over approximately 50 min of data rather than 1 day. From examination of the 22:35–23:25 UT line, the IAR peaks are consistent in terms of Δf and magnitude from 2 to 14 Hz. This may be interpreted as the IAR superposed across the SR in the time domain rather than interacting directly via another physical mechanism.

To check this hypothesis, we examined the raw time domain data to see if there are any obvious interference patterns in the digitizer data (not shown). We plotted 100 s worth of Butterworth-filtered digitizer data from 14:45 UT, 22:35 UT on 2 December and 02:25 UT on 3 December 2013. Though there are some larger values in the 14:45 UT data, typically associated with large lightning strikes, the general characteristics of each data set were similar, implying no obvious differences between the time periods chosen.

3.1. Occurrence Statistics of IAR and Their Superposition With SR

We analyzed 61 months of data from the start of September 2012 to end of September 2017, generating 1,765 complete spectrograms. For each of these we visually inspected the image and noted occasions when IAR both (a) occurred and (b) showed obvious interference with SR. We also observed pulsations as well as sporadic man-made interference within the data set. In general, IAR occur in approximately half the days examined (900 days) with seasonal and interannual variation. For example, there are only 94 days with IAR in 2014, but this rises to 247 days in 2016 (see Table 1).

We found 148 instances of IAR interference with the SR over the 5 years studied, again with seasonal and year-to-year variation. For example, only 11 days with both criteria (a) and (b) were observed in 2014 but 42 were found in 2016 and 33 in 2017. Occurrence is typically in winter time from September to March, though there are rare occasions in summer time when they are seen. We also noted 137 days with clear Pc1-type pulsation activity. Table 1 shows the occurrence of each phenomena in each calendar year, though recall only part of 2012 and 2017 are available.

Figure 4 shows a collection of statistical comparisons of the occurrence of all IAR days, days when IAR are seen to interact with SR (IAR/SR) and Pc1 pulsations. We compare the observations of IAR to geomagnetic activity

Table 1
Number of Missing Days of Data and the Occurrence of IAR, IAR Interacting with SR, and Pc1 Pulsations in Each Year

Year	2012[a]	2013	2014	2015	2016	2017[b]	Total
Missing days	11	0	44	24	0	12	91
IAR	69	179	94	134	247	177	900
IAR/SR	17	27	11	18	42	33	148
Pulsations	2	15	7	53	44	16	137

[a]From September only. [b]To October only. IAR = ionospheric Alfvén resonances; SR = Schumann resonances.

using the Dst and Kp indices and examine the occurrence over time. To make the comparison with each day, the 24 Dst values were averaged to a single value for the day and the minimum of the day was also selected. For the Kp index comparison, the mode (i.e., most likely value) of the Kp index and the maximum of the 8 Kp values for each day were selected.

The first and second panels of Figure 4 show that the IAR can occur in conditions of low to medium geomagnetic activity (Dst > -50 nT and up to Kp of 4). The occurrence of IAR interacting with SR tends to be in quieter conditions, typically Dst > -20 nT and Kp of 3 or lower. Pulsations occur across a wider range of activity, up to Kp of 8. However, though large pulsation events are usually triggered by geomagnetic storms, there is often several days' lag before they fully disappear, by which time global activity has declined.

The third panel of Figure 4 shows the occurrence rate of each phenomenon per calendar month (as a percentage of the total number observed), averaged across the 5 years sampled. For example, IAR interfering with SR (IAR/SR) occur 31% of the time in January but are not recorded in May. IAR occur every month though are more common in winter time. Pulsations occur all year, with the large peak in March related to the March 2013 and 2015 storms. The fourth panel shows the occurrence of each features as a percentage of the number of days in each month over the 5 years of data. The appearance of IAR show strong seasonality from 2012 to 2015, with a marked decline in 2015. From 2016 onward they are occasionally visible during summer and become ubiquitous in winter of 2016/2017 being visible almost 100% of the time. Note that geomagnetic activity peaks around the equinoxes because of the Russell-McPherron effect as a consequence of solar system geometry. It also lags behind the solar cycle by several years, as seen in many indices.

One further observation to note is that the IAR and pulsation occurrence rates appear to be out of phase. A weak correlation with the geomagnetic activity cycle can be argued for the pulsations, which peaked in 2016. The solar cycle peaked in April 2014 but the IAR show a minimum in the following year, perhaps suggestive of a time lag. A strong correlation with geomagnetic activity has been observed by other researchers (e.g., Baru et al., 2016; Potapov et al., 2014) but is not quite so obvious here. As this is a long-term research project, we intend to continue collecting data to further improve this part of the analysis.

3.2. Examples of Unusual Superpositions

We now illustrate some of the more unusual IAR and SR superposition features that have been observed in the spectrograms. These are features that have not been documented elsewhere, as far as is known, and show unexplained behavior of the IAR. Figure 5 shows six example spectrograms, which we next describe:

16 December 2012. The top left panel shows the spectrogram from 12:00 UT 15 to 16 December 2012. This day shows faint IAR with very straight, fixed frequency bands and regular Δf throughout the period. There is faint IAR interference with the first three SR during the hours of 23:00–01:00 UT. This example illustrates that Δf can remain very stable for periods of 10 or more hours, which is not typically seen in IAR.

27 December 2015. The top right panel shows an unusual cooccurrence of IAR interacting with the first two SR during a Pc1 pulsation event. The pulsations can be seen as the intense features at around 1–3 Hz between 03:00 and 09:00 UT. Hence, there are three separate ionospheric-magnetospheric wave systems observed during the period of 03:00–04:00. This suggests that there is no direct link between each of these phenomena and they can coexist (albeit briefly) without obvious feedback.

15 January 2016. The middle left panel illustrates a nonlinear set of IAR with f variations in a "wavy" pattern. The IAR behavior between 02:00 UT and 07:00 UT shows a gradual decrease of the IAR frequencies by around 1.5 Hz

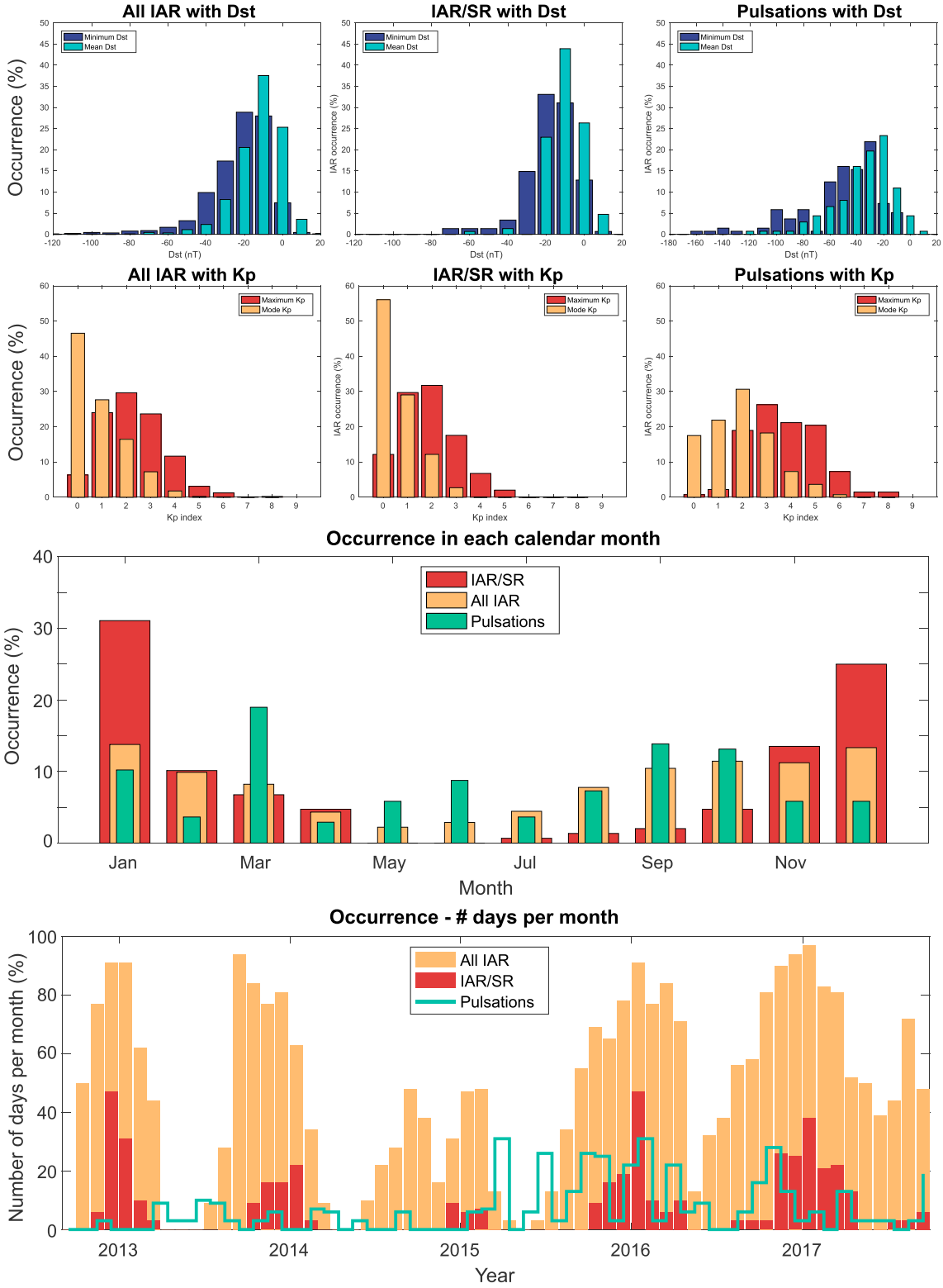

Figure 4. Histograms of the occurrence of all IAR, IAR interfering with SR (IAR/SR), and pulsation activity with respect to the Kp and Dst indices from September 2012 to September 2017. (first row) Occurrence versus Dst index; (second row) occurrence versus Kp index; (third row) occurrence versus calendar month; (fourth row) occurrence as a percentage of days per month from September 2012 to September 2017.

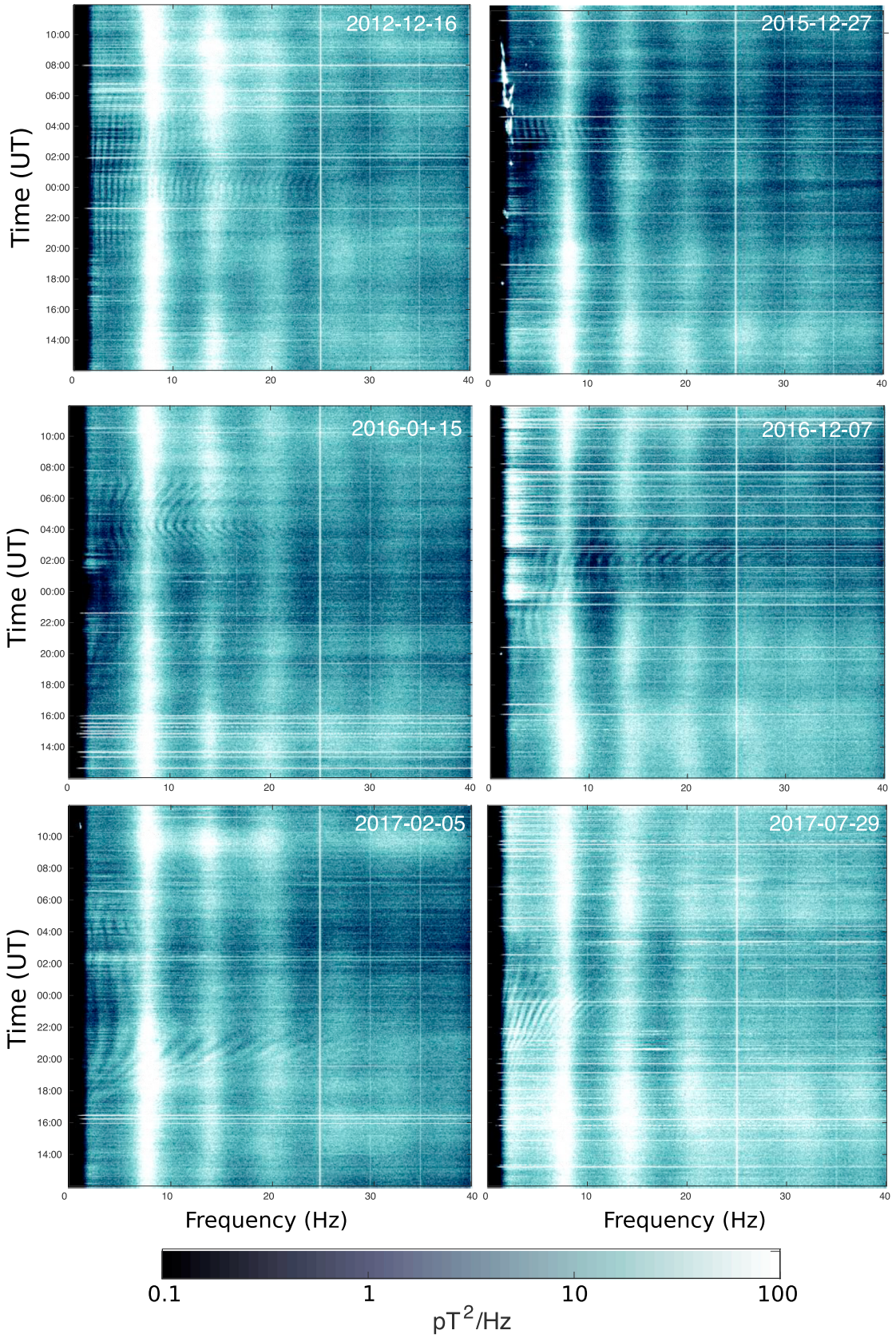

Figure 5. Examples of IAR interacting with SR from 2012 to 2017. See text for details.

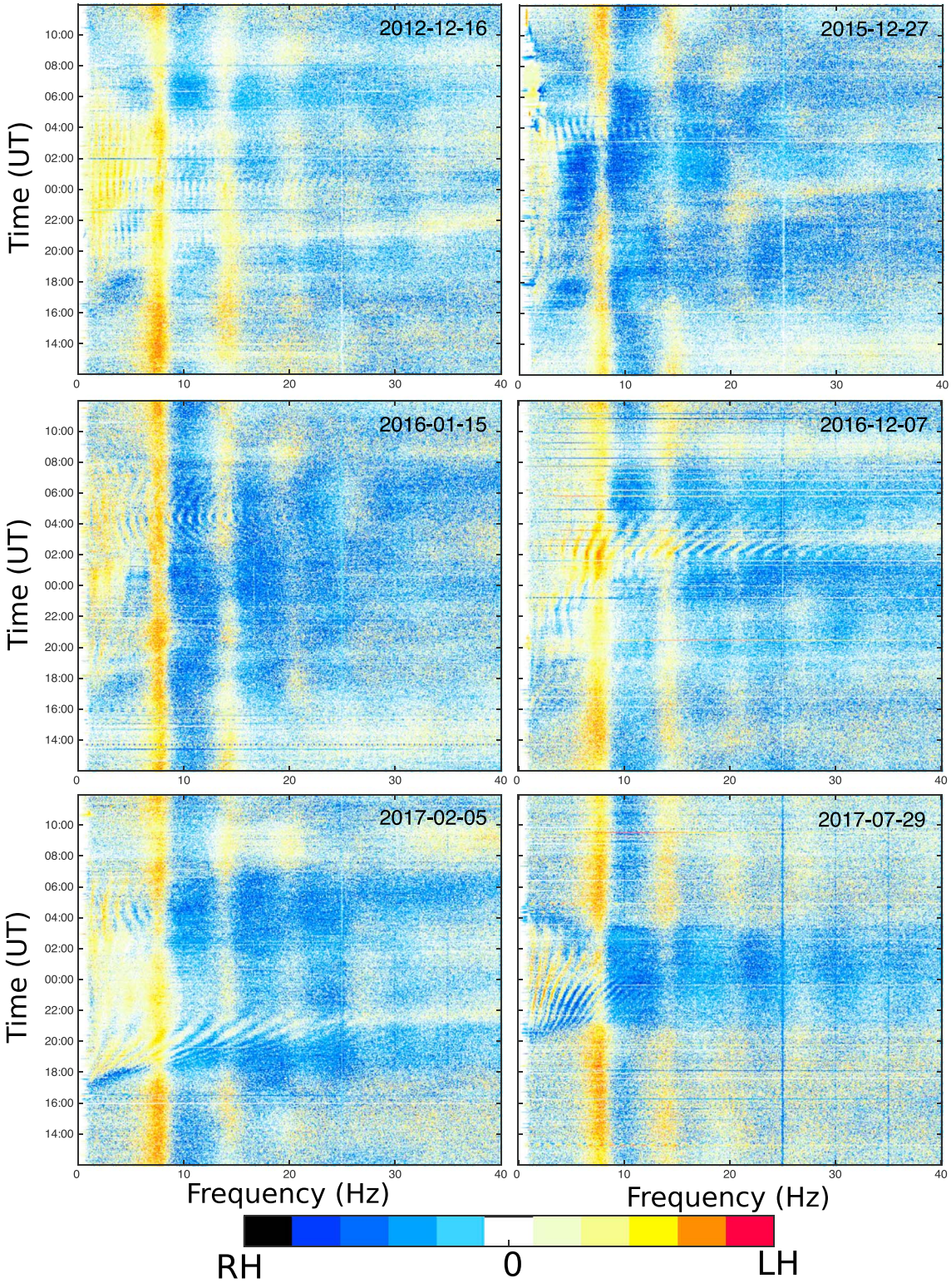

Figure 6. Ellipticity plots for each of the days in Figure 5. Left-hand polarity is positive; right-hand polarity is negative.

before recovering back to the initial value. This occurs over a period of around 5 hr. The Δf does not appear to change within the "wavy" pattern, suggesting that the ionospheric "thickness" did not vary significantly (cf. Hebden et al., 2005).

7 December 2016. The middle right panel shows a relatively noisy period (i.e., strong horizontal lines) related to regional lightning activity in Europe to which the coils are sensitive. However, this is one of the few occasions where the IAR can be observed to reach up to 30 Hz between 01:00 and 03:00 UT.

5 February 2017. The bottom left panel displays a series of very strong IAR that cross SR relatively early in the local evening at 18:00–20:00 UT, as compared to the other panels when this occurs later in the night. The IAR appear to interact intensely with the SR causing first SR to develop pronounced extensions and embayments around 20:00 UT. The IAR also reach 30 Hz before fading at 22:00 UT above 8 Hz.

29 July 2017. The bottom right panel shows a summer time example of the IAR interacting with the SR. This spectrogram shows IAR with small Δf crossing the first and second SR around 21:30 UT to 02:00 UT. Local sunset is around 20:20 UT and sunrise is 04:15 UT in late July, though at such high latitudes the Sun does not dip more than 16° below the horizon at the surface.

Figure 6 plots the ellipticity of the measured phenomena on each of the six selected days. The elliptogram plots are computed using the formulation in Sentman (1987). Positive ellipticity is defined as being left-handed and negative ellipticity is right-handed, following the convention of Nosé et al. (2017), for example. As can be observed, the SR are always positive, showing a peak between 12:00 and 18:00 UT. The IAR are denoted by a series of alternating fringes of positive and negative polarity. The different days show various superposition behaviors between the IAR and SR. On 6–7 December 2016 (middle right panel), the IAR produce a strong positive ellipticity as they cross the first SR around 00:00–02:00 UT, whereas on 28/29 July 2017 (lower right panel), the IAR pass straight across first SR causing primarily destructive interference.

3.3. Comparison With f_0F_2 Variation

We have shown seven examples of IAR interacting with SR over a 5-year period. These examples (from a total of 148) display some of the more unusual superpositions observed in the induction coil data. Studies by Hebden et al. (2005), Parent et al. (2010), and Potapov et al. (2014) show that the critical frequency of the ionosphere (f_0F_2) is strongly correlated with IAR f and Δf. The f_0F_2 parameter (in MHz) is related to electron density, N_e, via the equation $f_0F_2 = 8.98 \cdot 10^{-3}\sqrt{N_e}$, where density is in cm^{-3}. Thus, f_0F_2 measurements act as a proxy for ionospheric conditions controlling the IAR.

To examine the ionospheric conditions during these selected days, we compared a set of selected IAR fringes from each of the six examples shown in Figure 5 to f_0F_2 data measured by two independent ionosondes in the United Kingdom. The Fairford ionosonde (operated by the USAF) is located in Gloucestershire, England (51.7°N, −1.5°E) approximately 415 km south of Eskdalemuir. The Chilton ionosonde (operated by Rutherford Appleton Laboratory) is located near Oxford, England (51.5°N, −0.6°E), around 450 km south of Eskdalemuir and 65 km east of Fairford. We obtained f_0F_2 data from the Global Ionospheric Radio Observatory website using their RESTful webservice API (Reinisch & Galkin, 2011).

From the six example days, we hand-picked a single-representative IAR fringe from the spectograms in order to compare its variation with time to the f_0F_2 measurements. Potapov et al. (2014) demonstrated that the relationship is linearly inversely with $f_{\mathrm{IAR}} \approx -0.4 \cdot f_0F_2$, implying we should see a similar trend between an IAR fringe and f_0F_2 by plotting the IAR on an inverted scale.

Figure 7 shows the f_0F_2 data from Chilton and Fairford ionosondes. The ionosonde readings are relatively noisy, with Chilton showing greater variability. It also appears that the Chilton ionosonde has a lower measuring limit of 2 MHz. Fairford data are generally smoother, though with a spike at 04:00 UT on 29 July 2017. The measurements agree within 1 MHz, in general.

The ionospheric conditions are similar on most of the days in winter. The f_0F_2 values fall from around 8 MHz during the daylight hours to around 2–3 Hz at twilight (typically 17.00–18.00 in December and January) as recombination occurs. The f_0F_2 rise by a few MHz until after midnight before falling slowing again. At dawn, the f_0F_2 rise again to over 8 MHz as sunlight begins to reionize the atmosphere (Fedorov, Mazur, Pilipenko, & Ermakov, 2016). The IAR fringe values, selected by hand by picking a single-representative fringe from each of the six spectrograms, are shown as black points on an inverted scale in hertz (values on the right-hand axis). According to Potapov et al. (2014) we should expect to see strong correlation between the shape of the f_0F_2

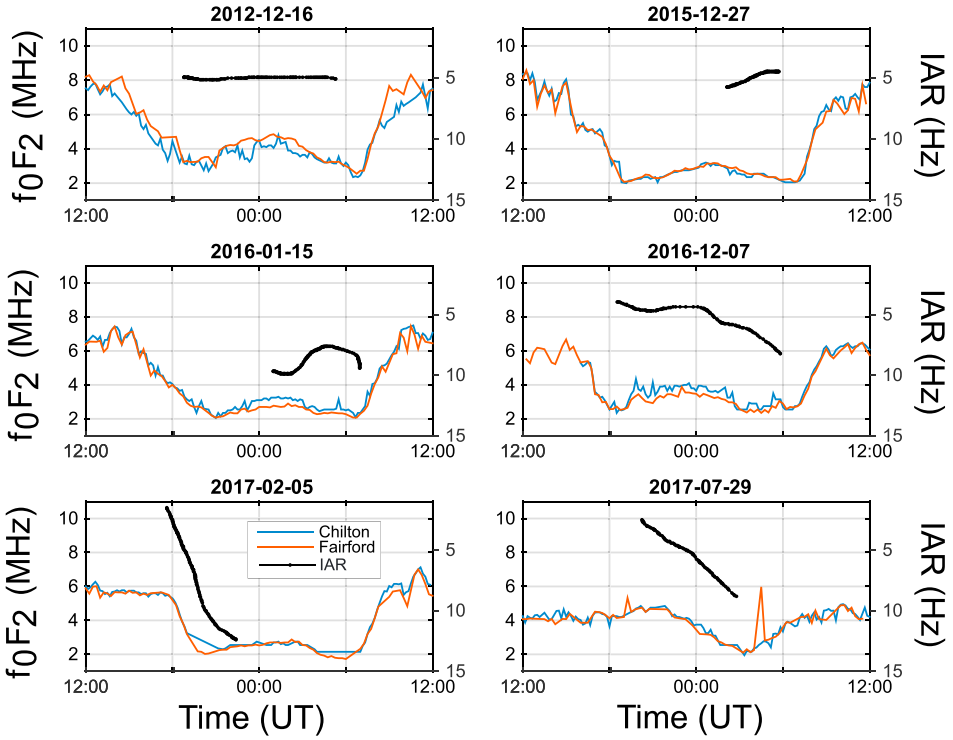

Figure 7. Plots of f_0F_2 data (in MHz) from the Chilton and Fairford ionosondes compared to a single hand picked IAR fringe (in Hz) selected from the spectrograms of the six example days.

and the inverted IAR fringes. However, this is not so obvious in the chosen examples. Three of the days (top left, top right, and middle left) show no real relation to the ionosonde measurements. The other three panels do visually correlate to the f_0F_2 variations during the parts of the day shown. However, the relationship is not particularly strong.

4. Discussion

The results of our investigations have confirmed many of the major findings of previous research with regard to the general behavior and morphology of the IAR. The 5 years of induction coil data have allowed us to explore the seasonal and longer-term variation of IAR occurrence. The primary novelty in this study lies in the observation of more complex IAR phenomena that have not been previously described (to our knowledge) in detail.

Figures 2 and 3 show the magnitude of both the SR and the IAR fringes. The SR decrease in magnitude during the local nighttime as the Sun passes across the Pacific Ocean where fewer lightning storms are triggered. During this time, the IAR become visible within the SR frequency ranges. The magnitude of the first SR reaches around 10 pT/$\sqrt{\text{Hz}}$ in the local afternoon, decreasing to about 6 pT/$\sqrt{\text{Hz}}$ by midnight. At this time, the IAR with magnitudes of ~1 pT/$\sqrt{\text{Hz}}$ appear. The IAR can be seen as a series of peaks climbing up the side of the main SR peaks and reappearing in the "dead" zones between resonances. In Figure 3, the 22:35–23:25 UT plot (red line) suggests that the IAR remain relatively constant in magnitude from 3 Hz to 12 Hz, once the SR is accounted for. This observation is in disagreement with much of the modeling work on IAR, which usually suggest a rapid decrease of IAR magnitude with frequency (e.g., Fedorov, Mazur, Pilipenko, & Engebretson, 2016; Fedorov, Mazur, Pilipenko, & Baddeley, 2016). However, Schekotov et al. (2011) and Fedorov, Mazur, Pilipenko, and Baddeley (2016) suggest alternative mechanisms for IAR related to generation of fields from local lightning storms within 1,000 km.

We have shown that the superposition of IAR with SR is relatively common, being observed around one sixth of the time that IAR are visible. IAR themselves are observed approximately half of the time at Eskdalemuir. The seasonal and solar cycle variation of the IAR at midlatitudes is well known and our results are consistent with

previous work (e.g., Molchanov et al., 2004), showing the IAR are most prominent in Northern Hemisphere winter and less likely to occur in summer (Figure 4). The superposition of IAR with SR is also most common in winter time. The occurrence rate showed a minimum in winter 2014/2015 of around 10% of days in December but increased to around 35–40% in the following 2 years (bottom panel). This suggests a link to the solar or geomagnetic activity cycle, though there is not yet sufficient data to fully confirm this.

The Kp and Dst comparisons shown in Figure 4 indicate a dependence of IAR occurrence on geomagnetic activity, particularly as IAR superposition with SR only appear under quiet conditions (when the mode of $Kp \leq 3$). IAR, in general, can arise in a slightly wider geomagnetic activity range (mode of $Kp \leq 4$). This does contradict the findings of Nosé et al. (2017) who found no IAR dependence on Kp. However, they examined a shorter data set of around 2.8 years. On the other hand, Molchanov et al. (2004) declared that an anticorrelation was found with the Kp index, though the dependence was not quantified.

Figure 6 examines the ellipticity of the SR and IAR. The ellipticity is always positive (left-handed) for SR, which may relate to the location of Eskdalemuir, on the opposite side of the Earth to the Pacific Ocean. Consequently, the IAR are usually visible during the quiescent period of the day (22:00–06:00 UT) when the magnitude of the SR declines overall. Other sites where IAR have been observed (e.g., Molchanov et al., 2004; Nosé et al., 2017, in Asia) make their measurements at local nighttime around 12:00–18:00 UT, which is during the hours of peak SR magnitude.

The IAR generally appear as a series of positive and negative fringes or spectral bands in polarization plots. The interaction between the resonances seems to increase polarity in some cases (e.g., 7 December 2016) but decreases it in others (e.g., 29 July 2017). As such, it is not clear whether simple wave superposition is occurring or there are other interactions between the resonances, such as wave coupling. Both the SR and IAR have been detected in the electric field at ELF by the C/NOFS satellite in low Earth (400–850 km), low inclination (13°) orbit (Simões et al., 2011, 2012). These observations support the "leaky" cavity interpretation and may allow the resonances to interact within the ionosphere itself. However, from the point of view of an observer on the ground in Eskdalemuir, one set of EM waves arise from horizontal propagation in the Earth-ionosphere cavity, while the other set is from almost vertically inclined waves. Hence, direct "beating" of each source at the ELF frequencies would be sufficient to generate the observed superposition. Given that we only have two horizontal sensors, additional information such as from a vertical antenna might be useful in resolving the ambiguity.

In Figure 7, the f_0F_2 measurements from two UK ionosondes are compared against a selected representative IAR fringe from the spectrograms in Figure 5. The time periods chosen are specific examples of unusual activity in IAR, and the spectral fringes show behaviors such as crossing SR or changing frequency in a nonlinear manner over periods of several hours. However, when the IAR are compared to the f_0F_2 data, the plots do not show unusual activity or variation within the ionosphere conductivity to suggest that this was the cause of the changes within the IAR. Though Potapov et al. (2014) and Potapov et al. (2017) give evidence of a linear relationship between f_0F_2 and IAR, this is not observed in Eskdalemuir on the highlighted days.

We note that Ermakova et al. (2013) attempted to model low-frequency (1–8 Hz) IAR features observed in Crete by Bösinger et al. (2002, 2004) based on a layered ionospheric model but also failed to fully describe the measurements. The modeling by Schekotov et al. (2011) may be able account for the high-frequency fringes observed above 8 Hz, though this relies on the occurrence regional lightning storms to enhance the IAR.

It appears that theoretical and modeling work needs to be refined to better understand the observed IAR variations. We will continue to collect more induction coil measurements to confirm these findings. Future work will also examine correlation between f_0F_2 and the Δf variation in more detail across the 5 years, for example, using the image processing techniques from Beggan (2014).

5. Conclusions

Induction coils at Eskdalemuir Observatory in the United Kingdom have been recording magnetic field variations in the ELF band (0.1–100 Hz) between September 2012 and September 2017. The coils have observed the Schumann resonances and ionospheric Alfvén resonances, as well as magnetospheric pulsations. We visually assessed the IAR and found them to extend to 30 Hz on occasion and to strongly superimpose over the SR, including constructive interference with the first three resonances. IAR are found to maintain a relatively

constant magnitude across frequencies which disagrees with much of the theoretical modeling work in the literature.

We investigated the occurrence statistics of the IAR, IAR found to interact with SR and pulsations, and noted their dependence on season and geomagnetic activity. We examined seven particular days with unusual IAR features and computed the ellipticity from the magnetic data. Finally, we compared the IAR frequencies to independent measurements of ionospheric f_0F_2 parameter from two UK ionosondes, finding little direct correlation between them. We suggest that further theoretical modeling and observations are needed to understand the IAR phenomena documented in this study.

Acknowledgments
We thank Chris Turbitt, Tony Swan, and Tim Taylor for their support in operating and maintaining the instrumentation at Eskdalemuir Observatory, United Kingdom, and Alan Thomson for commenting on an early draft. We thank Ian Mann for his suggestion to examine f_0F_2 data. This paper uses Fairford ionospheric data from the USAF NEXION Digisonde network, the NEXION Program Manager is Mark Leahy. We also acknowledge the use of Chilton ionsonde data operated by the Rutherford Appleton Laboratory. The f_0F_2 data were obtained from Global Ionospheric Radio Observatory (GIRO) and we acknowledge GIRO principal investigator B. W. Reinisch of the University of Massachusetts Lowell for making these data files available. The induction coil data, along with metadata and example MATLAB code can be found at http://www.bgs.ac.uk/services/NGDC/citedData/catalogue.html using the following DOIs to access the yearly data sets: 2012: https://doi.org/10.5285/6dcca520-47f2-45bd-9fd1-61354450d17d; 2013: https://doi.org/10.5285/6c18b97e-860a-4c47-8872-bedbe953c2ab; 2014: https://doi.org/10.5285/397aa96c-3377-3377-4039-a417-3111f1522214; 2015: https://doi.org/10.5285/c09b051d-94ac-4aec-a49f-34d8b4cd1327; 2016: https://doi.org/10.5285/aaf20915-1c3e-40f3-bc00-dafe593ff9e5, and 2017: https://doi.org/10.5285/25de906d-a3cd-4d64-8644-77f98aafeba6. This paper is published with the permission of the Executive Director of the British Geological Survey (NERC).

References

Anyamba, E, Williams, E., Susskind, J., Fraser-Smith, A., & Füllekrug, M. (2000). The manifestation of the Madden-Julian Oscillation in global deep convection and in the Schumann resonance intensity. *Journal of the Atmospheric Sciences*, *57*(8), 1029–1044. https://doi.org/10.1175/1520-0469(2000)057<1029:TMOTMJ>2.0.CO;2

Baru, N., Koloskov, A., Yampolsky, Y., & Rakhmatulin, R. (2016). Observations and analysis of the ionospheric Alfven resonance mode structure in a complete 11-year solar cycle. *Sun and Geosphere*, *11*, 49–54.

Beggan, C. D. (2014). Automatic detection of ionospheric Alfvén resonances using signal and image processing techniques. *Annales Geophysicae*, *32*(8), 951–958. https://doi.org/10.5194/angeo-32-951-2014

Belyaev, P. P., Bösinger, T., Isaev, S., & Kangas, J. (1999). First evidence at high latitudes for the ionospheric Alfvén resonator. *Journal of Geophysical Research*, *104*(A3), 4305–4317. https://doi.org/10.1029/1998JA900062

Belyaev, P. P., Polyakov, C. V., Rapoport, V. O., & Trakhtengerts, V. Y. (1989). Experimental studies of the spectral resonance structure of the atmospheric electromagnetic noise background within the range of short-period geomagnetic pulsations. *Radiophysics and Quantum Electronics*, *32*(6), 491–501. https://doi.org/10.1007/BF01058169

Belyaev, P. P., Polyakov, S., Rapoport, V., & Trakhtengerts, V. Y. (1990). The ionospheric Alfvén resonator. *Journal of Atmospheric and Terrestrial Physics*, *52*(9), 781–788. https://doi.org/10.1016/0021-9169(90)90010-K

Bösinger, T., Demekhov, A., & Trakhtengerts, V. (2004). Fine structure in ionospheric Alfvén resonator spectra observed at low latitude (L = 1.3). *Geophysical Research Letters*, *31*, L11802. https://doi.org/10.1029/2004GL020777

Bösinger, T., Haldoupis, C., Belyaev, P., Yakunin, M., Semenova, N., Demekhov, A., & Angelopoulos, V. (2002). Spectral properties of the ionospheric Alfvén resonator observed at a low-latitude station (L= 1.3). *Journal of Geophysical Research*, *107*(A10), 1281. https://doi.org/10.1029/2001JA005076

Ermakova, E. N., Kotik, D. S., Ryabov, A. V., Pershin, A. V., Bösinger, T., & Zhou, K. (2013). Studying the variations of the broadband spectral maximum parameters in the natural ULF fields. *Radiophysics and Quantum Electronics*, *55*(10), 605–615. https://doi.org/10.1007/s11141-013-9398-0

Fedorov, E., Mazur, N., Pilipenko, V., & Baddeley, L. (2016). Modeling the high-latitude ground response to the excitation of the ionospheric MHD modes by atmospheric electric discharge. *Journal of Geophysical Research: Space Physics*, *121*, 11,282–11,301. https://doi.org/10.1002/2016JA023354

Fedorov, E., Mazur, N., Pilipenko, V., & Engebretson, M. (2016). Interaction of magnetospheric Alfvén waves with the ionosphere in the Pc1 frequency band. *Journal of Geophysical Research: Space Physics*, *121*, 321–337. https://doi.org/10.1002/2015JA021020

Fedorov, E. N., Mazur, N. G., Pilipenko, V. A., & Ermakov, E. N. (2016). Modeling diurnal variations of the IAR parameters. *Acta Geodaetica et Geophysica*, *51*, 597–617. https://doi.org/10.1007/s40328-015-0158-9

Füllekrug, M. (1995). Schumann resonances in magnetic field components. *Journal of Atmospheric and Terrestrial Physics*, *57*(5), 479–484. https://doi.org/10.1016/0021-9169(94)00075-Y

Füllekrug, M., & Reising, S. C. (1998). Excitation of earth-ionosphere cavity resonances by sprite-associated lightning flashes. *Geophysical Research Letters*, *25*(22), 4145–4148. https://doi.org/10.1029/98GL02590

Greifinger, C., & Greifinger, P. S. (1968). Theory of hydromagnetic propagation in the ionospheric waveguide. *Journal of Geophysical Research*, *73*(23), 7473–7490. https://doi.org/10.1029/JA073i023p07473

Hebden, S. R., Robinson, T. R., Wright, D. M., Yeoman, T., Raita, T., & Bösinger, T. (2005). A quantitative analysis of the diurnal evolution of ionospheric Alfven resonator magnetic resonance features and calculation of changing IAR parameters. *Annales Geophysicae*, *23*(5), 1711–1721. https://doi.org/10.5194/angeo-23-1711-2005

Lysak, R. L. (1991). Feedback instability of the ionospheric resonant cavity. *Journal of Geophysical Research*, *96*(A2), 1553–1568. https://doi.org/10.1029/90JA02154

Lysak, R. L. (1993). Generalized model of the ionospheric Alfvén resonator. *Geophysical Monograph Series*, *80*, 121–128.

Mann, I., Milling, D., Rae, I., Ozeke, L., Kale, A., Kale, Z., et al. (2008). The upgraded CARISMA magnetometer array in the THEMIS era. *Space Science Reviews*, *141*, 413–451. https://doi.org/10.1007/s11214-008-9457-6

Molchanov, O., Schekotov, A., Fedorov, E., & Hayakawa, M. (2004). Ionospheric Alfven resonance at middle latitudes: Results of observations at Kamchatka. *Physics and Chemistry of the Earth Parts A/B/C*, *29*(4), 649–655. https://doi.org/10.1016/j.pce.2003.09.022

Nickolaenko, A. P., & Hayakawa, M. (2002). *Resonances in the Earth-ionosphere cavity* (Vol. 19). Springer Science & Business Media.

Nickolaenko, A. P., Koloskov, A. V., Hayakawa, M., Yampolski, Y. M., Budanov, O. V., & Korepanov, V. E. (2015). 11-year solar cycle in Schumann resonance data as observed in Antarctica. *Sun and Geosphere*, *10*(1), 39–49.

Nosé, M., Uyeshima, M., Kawai, J., & Hase, H. (2017). Ionospheric Alfvén resonator observed at low-latitude ground station, Muroto. *Journal of Geophysical Research: Space Physics*, *122*, 7240–7255. https://doi.org/10.1002/2017JA024204

Parent, A., Mann, I. R., & Rae, I. J. (2010). Effects of substorm dynamics on magnetic signatures of the ionospheric Alfvén resonator. *Journal of Geophysical Research*, *115*, A02312. https://doi.org/10.1029/2009JA014673

Potapov, A., Polyushkina, T., Dovbnya, B., Tsegmed, B., & Rakhmatulin, R. (2014). Emissions of ionospheric Alfvén resonator and ionospheric conditions. *Journal of Atmospheric and Solar-Terrestrial Physics*, *119*, 91–101. https://doi.org/10.1016/j.jastp.2014.07.001

Potapov, A., Polyushkina, T., Tsegmed, B., Oinats, A., Pashinin, A., Edemskiy, I., et al. (2017). Considering the potential of IAR emissions for ionospheric sounding. *Journal of Atmospheric and Solar-Terrestrial Physics*, *164*, 229–234. https://doi.org/10.1016/j.jastp.2017.08.026

Reinisch, B. W., & Galkin, I. A. (2011). Global ionospheric radio observatory (GIRO). *Earth, Planets, and Space*, *63*, 377–381. https://doi.org/10.5047/eps.2011.03.001

Sátori, G. (1996). Monitoring Schumann resonances—II. Daily and seasonal frequency variations. *Journal of Atmospheric and Terrestrial Physics*, *58*(13), 1483–1488. https://doi.org/10.1016/0021-9169(95)00146-8

Sátori, G., Williams, E., & Mushtak, V. (2005). Response of the Earth-ionosphere cavity resonator to the 11-year solar cycle in X-radiation. *Journal of Atmospheric and Solar-Terrestrial Physics*, *67*(6), 553–562. https://doi.org/10.1016/j.jastp.2004.12.006

Schekotov, A., Pilipenko, V., Shiokawa, K., & Fedorov, E. (2011). ULF impulsive magnetic response at mid-latitudes to lightning activity. *Earth Planets Space*, *63*, 119–128. https://doi.org/10.5047/eps.2010.12.009

Schumann, W. O. (1952). Über die strahlungslosen Eigenschwingungen einer leitenden Kugel, die von einer Luftschicht und einer Ionosphärenhülle umgeben ist. *Zeitschrift für Naturforschung A*, *7*(2), 149–154.

Sentman, D. D. (1987). Magnetic elliptical polarization of Schumann resonances. *Radio Science*, *22*(4), 595–606. https://doi.org/10.1029/RS022i004p00595

Simões, F., Klenzing, J., Ivanov, S., Pfaff, R., Freudenreich, H., Bilitza, D., et al. (2012). Detection of ionospheric Alfvén resonator signatures in the equatorial ionosphere. *Journal of Geophysical Research*, *117*, A11305. https://doi.org/10.1029/2012JA017709

Simões, F., Pfaff, R., & Freudenreich, H. (2011). Satellite observations of Schumann resonances in the Earth's ionosphere. *Geophysical Research Letters*, *38*, L22101. https://doi.org/10.1029/2011GL049668

Welch, P. D. (1967). The use of Fast Fourier Transform for the estimation of power spectra: A method based on time averaging over short, modified periodograms. *IEEE Transactions on Audio and Electroacoustics*, *15*(2), 70–73. https://doi.org/10.1109/TAU.1967.1161901

Williams, E. R. (1992). The Schumann resonance: A global tropical thermometer. *Science*, *256*(5060), 1184–1187. https://doi.org/10.1126/science.256.5060.1184

Yahnin, A., Semenova, N., Ostapenko, A., Kangas, J., Manninen, J., & Turunen, T. (2003). Morphology of the spectral resonance structure of the electromagnetic background noise in the range of 0.1–4 Hz at L = 5.2. *Annales Geophysicae*, *21*(3), 779–786. https://doi.org/10.5194/angeo-21-779-2003